# Nanoscale

## Anti-tumor effect of pH-sensitive drug–loaded nanoparticles optimized via an integrated computational/experimental approach

SCHOLARONE™
Manuscripts

**Anti-tumor effect of pH-sensitive drug-loaded nanoparticles optimized via an integrated computational/experimental approach**

Hunter A. Miller[a,+], Yapei Zhang[b,c,+], Bryan Ronain Smith[b,c,*], Hermann B. Frieboes[a,d,e,f,*]

[a] Department of Bioengineering, University of Louisville, Louisville, KY, USA

[b] Department of Biomedical Engineering, Michigan State University, East Lansing, MI, USA

[c] Institute for Quantitative Health Science and Engineering, Michigan State University, East Lansing, MI, USA

[d] Department of Pharmacology and Toxicology, University of Louisville, Louisville, KY, USA

[e] James Graham Brown Cancer Center, University of Louisville, Louisville, KY, USA

[f] Center for Predictive Medicine, University of Louisville, Louisville, KY, USA

[+] Equal contribution

[*]**Co-corresponding authors:**

Hermann B. Frieboes: hbfrie01@louisville.edu

Bryan R. Smith: smit2901@msu.edu

**ABSTRACT**

The acidic pH of tumor tissue has been used to trigger drug release from nanoparticles. However, dynamic interactions between tumor pH and vascularity present challenges to optimize therapy to particular microenvironment conditions. Despite recent development of pH-sensitive nanomaterials that can accurately quantify drug release from nanoparticles, tailoring release to maximize tumor response remains elusive. This study hypothesizes that a computational modeling-based platform that simulates the heterogeneously vascularized tumor microenvironment can enable evaluation of the complex intra-tumoral dynamics involving nanoparticle transport and pH-dependent drug release, and predict optimal nanoparticle parameters to maximize the response. To this end, SPNCD nanoparticles comprising superparamagnetic cores of iron oxide ($Fe_3O_4$) and a poly(lactide-co-glycolide acid) shell loaded with doxorubicin (DOX) were fabricated. Drug release was measured *in vitro* as a function of pH. A 2D model of vascularized tumor growth was calibrated to experimental data and used to evaluate SPNCD effect as a function of drug release rate and tissue vascular heterogeneity. Simulations show that pH-dependent drug release from SPNCD delays tumor regrowth more than DOX alone across all levels of vascular heterogeneity, and that SPNCD significantly inhibit tumor radius over time compared to systemic DOX. The minimum tumor radius forecast by the model was comparable to previous *in vivo* SPNCD inhibition data. Sensitivity analyses of the SPNCD pH-dependent drug release rate indicate that slower rates are more inhibitory than faster rates. We conclude that an integrated computational and experimental approach enables tailoring drug release by pH-responsive nanomaterials to maximize the tumor response.

**KEYWORDS:** pH-sensitive nanoparticles, pH-dependent drug release, breast cancer, computational tumor modeling, nanomedicine

## INTRODUCTION

Nanoparticles have emerged as a promising tool with a wide range of potential medical applications including diagnosis, imaging, and therapy (1-3) and have boosted cancer therapy, efficacy, and safety in preclinical and clinical studies (4). Several pathological characteristics influence the tumor response to nanoparticle-mediated drug delivery, including vascular heterogeneity, tissue acidity, and immune interactions (5). By understanding these characteristics for particular tumors, nanoparticles can be tuned to release anticancer drugs to more specifically target the tumor environment and optimize therapy (6). Tumor tissue typically has lower pH than normal tissue due to the Warburg Effect (7), which yields lactate, an acid, during anaerobic glycolysis. Accordingly, many pH-sensitive nanoparticles have been designed to release their payload in the acidic tumor microenvironment in order to increase local dosage while reducing off-target effects in normal (non-acidic) tissue (8-10).

It has proven challenging to understand, and thus to optimally design, pH-dependent nanoparticle drug release because of differences across local tumor conditions —particularly due to dynamic interactions between tissue pH and vascularity (11).  We recently developed a pH-sensitive nanomaterial that enables accurate quantification of drug release from nanoparticles deep within breast tumors, which is made possible by exploiting the unique physical properties of magnetic particle imaging (MPI) in concert with superparamagnetic $Fe_3O_4$ nanocluster@poly(lactide-co-glycolide acid) core−shell nanocomposites loaded with chemotherapeutic drugs (12). The approach is based on the fairly-new, high-penetration depth imaging modality MPI, which directly images superparamagnetic iron oxide particles (SPNs) to produce MPI signal (13) and enables drug release quantification. The linearly quantifiable signal at low magnetic fields makes the MPI and SPN combination ideal to provide quantitative *in vivo* measures of nanoparticle-mediated drug release (12). In this paradigm, clustered superparamagnetic cores of iron oxide ($Fe_3O_4$) nanoparticles and a poly(lactide-co-glycolide

acid) (PLGA) shell comprise SPNC; loading the common chemotherapy doxorubicin then yields SPNCD. In the tumor acidic environment (pH ~6.5), SPNCD simultaneously release DOX and iron oxide NPs, producing linearly correlated signal. Importantly, the SPNCD nanocomposite releases drug based on the pH but remains stable at the neutral pH in normal tissue (12).

Yet despite success in development of this drug release monitoring technology, the specific parameters such as the drug release rate with which to design and tune the nanocomposites remain unclear to maximize the tumor response. Vascular heterogeneity across and within breast tumors may require this release to be customized; ideally, the NP design would be evaluated and tuned prior to treatment. Optimized pH-dependent release rates are a function of several key tumor-specific parameters, including vascularity that affects oxygenation and tissue pH. Moreover, it is important to account for the fact that the particle itself degrades into constituents that contribute to the acidic microenvironment in a potentially self-propelling degradation mechanism (12). Analysis of such complex system dynamics involving nanoparticle transport and pH-dependent drug release in the heterogeneously-vascularized tumor microenvironment could benefit from, or even require, mathematical modeling and computational simulation (14). These tools have been employed to gain insight into tumor growth and treatment response (15). In particular, simulation of heterogeneously vascularized tumor growth allows evaluation of therapeutic response based on transport barriers and associated tissue conditions such as hypoxia and lactate build-up (16-20). Other models have provided pre-clinical insight into various nanotherapies (14, 15, 21, 22), including simulation of nanotherapy targeting non-small cell lung cancer lesions (23), tumor vasculature (24), and liver metastases (25). Anti-tumor performance of systemically administered pH-sensitive polymer nano-assemblies has been explored as a function of nano-assembly release profiles, tumor tissue vascularization, and associated levels of tissue acidity (26).

Despite this progress, an unfulfilled goal remains prediction of nanoparticle parameters (e.g.,

pH-dependent drug release) to maximize tumor response as a function of complex intra-tumoral

dynamics including nanoparticle transport and vascularity. In this study, we advance this goal by

developing a computational modeling strategy that evaluates intra-tumoral injection of SPNCD

as a means for controlled nanotherapy assessment and then comparing the results to current

experimental data. We aim to provide a means to assess pH-dependent nanotherapy based on

the drug release rate from nanoparticles, and thereby to extract key nanomaterial design

considerations to optimize therapy. This study emphasizes the utility of applying experimentally

derived adjustable parameters in mathematical modeling of drug delivery to evaluate and

potentially improve pH-dependent cancer nanotherapy response.

**EXPERIMENTAL**

**Preparation of SPNCD**

Following our previous fabrication strategy (12), $Fe_3O_4$ nanoparticles (Imagion, 25 nm, 1 mg) were mixed with 5 mg PLGA (Millipore Sigma, Molecular weight: 4000 – 15000 Da) in 1 mL chloroform to form a mixture. The mixture was transferred to 4 mL of 3% (W/V) PVA (Millipore Sigma, Molecular weight: 13,000-23,000 Da) aqueous solution. After vortex and sonication, the emulsified solution was injected dropwise into 20 mL of 1% (W/V) PVA aqueous solution. The emulsion was stirred overnight to evaporate chloroform and form nanoclusters. The obtained nanoclusters (SPNC) were washed with DDI water 3 times and then dispersed in DDI water. Doxorubicin (DOX)-loaded nanoclusters were prepared by mixing SPNC and DOX in DDI water (pH=7.4) and stirring for 24 h. The resulting SPNCD nanocomposites were separated by centrifugation at 6,000×g and washed with DDI water 3 times and then dispersed in DDI water. A Nanodrop (ND-ONE-W, USA) confirmed successful loading of DOX on SPNC.

**Characterization of SPNCD**

A Malvern Zetasizer (Malvern, UK) was used to characterize the diameter of SPNCD. Transmission electron microscopy (TEM) (JEOL 2200FS, Tokyo) and scanning electron microscopy (SEM) (JEOL 7500F, Tokyo) were used to characterize the morphology of SPNCD.

**SPNCD degradation at different pH**

The pH of SPNCD solution was adjusted to pH 7.1, 6.8, 6.0 and 5.5, respectively. 20 µL of the samples were taken out at specific timepoints (0, 1, 3, 6, 24 and 48 h) and added into 1 mL DDI water for the size measurement by using Malvern Zetasizer. SPNCD degradation was calculated by quantifying the DLS (dynamic light scattering) peak changes of each sample.

**Drug release from SPNCD at different pH**

An assay to test DOX release from SPNCD at pH 7.4, 7.1, 6.8, 6.5, 6.0 and 5.5 was conducted.

SPNCD were added to MINI Dialysis Devices (MWCO: 20K) and the volume of release medium

was 3 mL. At fixed timepoints from 1 h to 48 h, 2 µL of the outlet medium was removed to test

the rate of DOX release via Nanodrop UV-Vis spectroscopy (ND-ONE-W, USA). The cumulative

drug release (CDR) percentage was calculated by the following equation:

$$CDR (\%) = W_{released}/W_{loaded} \times 100\% \tag{1}$$

Here, CDR represents the cumulative drug release percentage, $W_{released}$ represents the mass of

released DOX in the release media, and $W_{loaded}$ represents the total mass of DOX.

### Localization of SPNCD within murine tumor tissue

All animal procedures were carried out in strict compliance with the guidelines of the Institutional

Animal Care & Use Committee (IACUC) and performed with the approval of Campus Animal

Resources of Michigan State University (IACUC#: PROTO202200377). As in our previous study

(12), SPNCD were intra-tumorally injected to allow for controlled nanotherapy assessment. The

localization of SPNCD in breast tumor tissue was evaluated using Prussian Blue staining. 4T1

triple-negative breast cancer cells were collected, centrifuged, and resuspended in PBS. 4T1

cells ($1\times10^6$ cells per mouse) were implanted into the mammary fat pads of six-week-old female

Balb/c mice. Orthotopic tumor-bearing mice were considered ready for *in vivo* studies when the

tumor volume reached >100 mm$^3$. The tumor volume was calculated by the following

equation: $V = W^2 \times L/2$, where W and L are width and length of the tumor measured by calipers,

respectively. Then the 4T1 tumor-bearing mice were intra-tumorally injected with SPNCD every

2 d for 15 d. Tumors were harvested on day 15, processed with Prussian blue staining, and

imaged by Digital Microscopy (Keyence VHX-6000) to spatially quantify localized iron oxide

nanoparticles.

### SPNCD washout *in vivo*

SPNCD (1.22 mg/kg DOX) were intravenously injected into Balb/c mice (six-week-old, female). At predetermined time points (0, 0.17, 0.5, 1, 2, 5, 9, 14 and 24 h post-injection), blood was collected from mouse retro-orbital plexus, then placed in Eppendorf tubes and centrifuged to obtain plasma at 10000 g for 10 mins. SPNCD concentration in the plasma was measured by Nanodrop (ND-ONE-W, USA). Percent injected dose (ID %) = (Concentration of SPNCD at specific timepoint / Initial SPNCD concentration) x 100%.

**Computational Model**

The computational model represents tumors as continuous tissue and the vasculature as discrete vessels, as previously described in (26-29). Briefly, within a growing tumor inside a 2D Cartesian coordinate system, regions of viable, hypoxic, and necrotic tissue arise over time due to the limited diffusion of oxygen and nutrients from local vessels. Neovascularization from a pre-existing capillary grid, stimulated by tumor angiogenic factors (TAF) produced by the hypoxic tissue, provides additional oxygen and nutrients to the tumor tissue, enabling further growth. The main parameters of the model are in **Table 1**.

**Simulation of Tumor Growth**

The tumor growth is described in (30). Briefly, tumor growth velocity is generally (non-dimensionally) represented using Darcy's law as:

$$v_{c} = -\mu \nabla P + x_E \nabla E \tag{2}$$

where $v_c$ is tissue velocity, $\mu$ is cell mobility cell-mobility encapsulating the net effects of cell-cell and cell-matrix adhesion, $P$ is oncotic pressure, $x_E$ is haptotaxis, and $E$ is extracellular matrix (ECM) density. Detailed descriptions of these parameters are in (26, 30). Overall tumor growth, measured as a function of velocity, can be represented as:

$$\nabla \cdot v_c = \lambda_p \tag{3}$$

where cell density is assumed to be constant in the proliferating region, and $\lambda_p$ is the non-dimensionalized net proliferation rate (defined in Equation 13 below).

## Simulation of Angiogenesis

Tumor-induced angiogenesis is simulated by coupling vessel growth with blood flow (31), where neo-vessel sprouts arise and grow towards a gradient of tumor angiogenic factors (TAF) released by hypoxic tissue. The tissue pressure and distance from a vascular source varies across the vascular grid and gives the tumor cells heterogeneous access to oxygen and nutrients (28, 30). The angiogenesis component has been previously described in (28, 30).

## Simulation of Tumor Vascular Heterogeneity

Vascular heterogeneity affects tumor growth and the ensuing production of lactate in the tumor microenvironment (32), which would affect the SPNCD drug release and the tumor response to the SPNCD.  Accordingly, the proportion of hypoxic and necrotic tissue and the extent of tissue vascularization were varied in the simulations by changing the response to tumor angiogenic factors, as in (33). Tumor vascularization due to angiogenesis was varied to simulate three distinct levels of vascular heterogeneity, labeled "LOW", "MEDIUM", AND "HIGH." The values for these levels and the associated tumor characteristics are summarized in **Table 2**. Due to the semi-stochastic angiogenesis model, replicates were employed to account for slight differences in simulated tumor characteristics and to allow for statistical comparisons. N=4 replicate tumors were computationally generated for each level of heterogeneity and subjected to each treatment.

## Simulation of Lactate Production (acidity)

Anaerobic glycolysis along with increased lactate production (leading to lower pH within tumor tissue) is known as the Warburg effect (34). This study implements lactate produced by

proliferating and hypoxic tumor cells and diffusing through the surrounding tissue. It is removed

from the environment by tumor uptake and washout through the vasculature. Lactate production

is represented as 2 moles of lactate obtained for every mole of glucose during anaerobic

respiration (35):

$$0 = \nabla \cdot (D_{Lac.}\nabla L) + \overline{\lambda}_{production}^{Lac.}(1 - L) - \overline{\lambda}_{washout}^{Lac.}(\mathbf{1}_{vessel}) - \overline{\lambda}_{uptake}^{Lac.}L \tag{4}$$

where $D_{Lac.}$ is lactate diffusivity, $L$ is local lactate concentration, $\overline{\lambda}_{production}^{Lac.}$ is production rate,

$\overline{\lambda}_{washout}^{Lac.}$ is washout rate, and $\overline{\lambda}_{uptake}^{Lac.}$ is cellular uptake rate. The lactate production rate is

dependent on the lactate concentration in the microenvironment, since cancer cells can adjust

their metabolic activity by altering the production to maintain a range of pH in their

microenvironment (36). The model assumes that lactate production $\overline{\lambda}_{production}^{Lac.}$ increases as the

level of oxygen $\sigma$ decreases in regions of lower vascularization (34)

$$\overline{\lambda}_{production}^{Lac} = \begin{cases} 1 - \sigma & in\ \Omega_P \\ 2\sigma & in\ \Omega_H \\ 0 & in\ \Omega_N \end{cases} \tag{5}$$

Since the high diffusivity of lactate (with values measured as ~3x10$^{-6}$ cm$^2$/s in agarose gel (37)

and ~1x10$^{-6}$ cm$^2$/s in muscle (38)) is close to that of oxygen (3.6x10$^{-5}$ cm$^2$/s in tissue (39)), the

diffusion constant $D_{Lac.}$ is for simplicity assumed to be similar to that of oxygen. Lactate is,

therefore, assumed to diffuse through the tissue relatively uninhibited by the extracellular matrix

(ECM), consistent with observations that lactate does not typically accumulate in tissue (34).

Similarly, the lower bound rate of lactate uptake is assumed to be on the same order of

magnitude as that of oxygen.


**Calibration of Drug Injection Amounts**

The recommended DOX hydrocholoride injection of 60 mg/m$^2$ body surface area for adjuvant

breast cancer was used to calculate the amount of DOX administered in the simulations (40).

Assuming an average female body surface area of 1.84 m$^2$ based on average height and weight

of females age 60 or older (41), a standard dose is 110.4 mg, which is equivalent to 44.26 µM once diluted in the average female plasma volume of 4.3 L (42). Accordingly, the amount of systemic DOX entering the computational domain from the vasculature was fixed to represent this (non-dimensionalized) concentration for the HIGH heterogeneity case and decreased proportionally to the amount of vasculature present in the MEDIUM and LOW heterogeneity cases.

**Simulation of Nanoparticle and Drug Transport**

SPNCD were injected intra-tumorally as a means for controlled nanotherapy assessment, and the effects were compared to the current standard of care (systemic bolus DOX) and a non-NP mediated control administration (intra-tumoral DOX). Both the amount of intra-tumorally injected DOX entering the simulated domain and the amount of encapsulated DOX for the intra-tumorally injected SPNCD were set to represent the non-dimensionalized values of these amounts regardless of tumor heterogeneity, equivalent to the standard dose of 110.4 mg for systemic therapy.

SPNCD transport through the tumor and host tissues was simulated from the point of injection at the tumor center and diffused through the tumor and surrounding host tissues with diffusivity $D_s$.

$$\frac{\partial s}{\partial t} = \nabla \cdot (D_s \nabla s) + \overline{S}_S(\mathbf{1}_{needle}) - \overline{\lambda}^s_{washout}(\mathbf{1}_{vessel}) \tag{6}$$

SPNCD concentration $s$ was initially $\overline{S}_S$ at the site of injection $\mathbf{1}_{needle}$. Diffusivity $D_s$ was set to 10 times (of normal diffusion) within 0.125 of the tumor area (~160 µm radius) from the injection site to achieve intra-tumoral distribution comparable to that observed *in vivo* (**Supplementary Figure 1**). SPNCD were assumed to washout through the vasculature $\overline{\lambda}^s_{washout}(\mathbf{1}_{vessel})$. The washout was fit to SPNCD measurements in blood circulation of mice (**Supplementary Figure 2**).

Drug $G$ was released from SPNCD in a time- and pH- dependent manner with rate $\lambda^G_{release}$, diffused through tissue with diffusivity $D_G$ and decayed with rate $\bar{\lambda}^G_{decay}$ assuming a 24 h half-life:

$$\frac{\partial G}{\partial t} = \nabla \cdot (D_G \, \nabla G) + \lambda^G_{release}(t, T_A) - \bar{\lambda}^G_{decay} \tag{7}$$

where $T_A$ represents non-dimensionalized tumor acidity by rescaling the value of lactate from 0 to 1. The amount of drug released over time was calibrated to the experimental data via a best fit equation (Equation 11 below).

During systemic bolus administration, drug extravasates from the vasculature with rate $\lambda_{G,ev}$ obeying the equation:

$$0 = \nabla \cdot (D_G \, \nabla G) + \lambda_{G,ev}(\mathbf{x}, t, \mathbf{1}_{vessel}, p_i, G) - \bar{\lambda}^G_{decay} \tag{8}$$

where $p_i$ is interstitial fluid pressure. The drug extravasation $\lambda_{G,ev}$ depends on the transfer rate $\lambda_{G,TR}$ from the vasculature (assumed constant over time):

$$\lambda_{G,ev} = \lambda_{G,TR}(\mathbf{1}_{vessel})(\mathbf{x},t)\left(1 - \frac{k_{p,i}p_i}{p_e}\right) \tag{9}$$

where $k_{p,i}$ represents the weight of the convective transport component of drug molecules and $p_e$ is effective pressure (28).

For comparison to SPNCD injection, drug was injected into the center of the tumor (acting as a source $\bar{G}_G$ of drug at the needle location $\mathbf{1}_{needle}$):

$$\frac{\partial G}{\partial t} = \nabla \cdot (D_G \, \nabla G) + \bar{G}_G(\mathbf{1}_{needle}) - \bar{\lambda}^G_{decay} \tag{10}$$

As with the injected SPNCD, diffusivity $D_G$ of drug molecules at the site of injection was set to 10 times the normal value within 0.125 of the tumor area (~160 µm radius) from the injection site to achieve intra-tumoral distribution comparable to that observed in real tumors subjected to intra-tumoral injection (43, 44).

**Simulation of pH-Dependent Drug Release**

As in (26), the pH-dependent drug release profiles from SPNCD were determined by fitting the experimental data of DOX released from SPNCD (**Supplementary Table 1**) to the equation:

$$N = [n_1 - (n_2 - T_A(n_2 - n_3))]e^{-(\alpha + \beta T_A)t} + (n_2 - T_A(n_2 - n_3)) - \gamma t(1 + (1 - T_A))^\varepsilon \quad (11)$$

where $N$ represents the cumulative fraction of drug remaining and $t$ is time. The parameter values used to fit the equation at each pH level are reported in **Supplementary Table 2**. The drug release is then found at each location in the domain as the rate of change of the cumulative fraction of drug remaining:

$$\lambda_{release}^G = \frac{\partial N}{\partial t} \quad (12)$$

Computationally, the release is determined by defining levels of pH (7.4, 7.1, 6.8, 6.5, 6.0, 5.5) as a function of the dynamic lactate production by the tumor tissue and calculating the drug release at that value over time. The discretization of pH is tracked over the entire spatial domain where a $T_A$ value of 0 represents minimum acidity (pH=7.4) and $T_A$ value of 1 represents maximum acidity (here, defined as pH=5.5). To perform a sensitivity analysis of the release rate's impact on tumor inhibition, a total of five SPNCD DOX release rate profiles were investigated. These included the experimental baseline, designated as "Rate 3", and 4 additional theoretical cases of slower, slowest, faster, and fastest release, designated as "Rate 1", "Rate 2", "Rate 4", and "Rate 5", respectively.

**Calibration of Simulated Drug Effect**

The drug-induced cell death $\bar{\lambda}_{effect}$ of doxorubicin (DOX) was calibrated by finding the rate that corresponded to the half-maximal inhibitory concentration (IC$_{50}$) using data from 3D culture of human breast cancer cells (MDA-MB-231) (45) employed in the experiments in (12) . The IC$_{50}$

was defined to represent 50% viable (proliferating and hypoxic) tissue reduction. The median (non-dimensionalized) value of DOX found across the computational domain during the 48 h therapy period was set to a concentration value of 77.35 μM based on the $IC_{50}$ observed with MDA-MB-231 cells (45). The values of DOX reported are scaled to this concentration.

**Simulation of Tumor Response**

It is assumed that only proliferating cells are sensitive to drugs (such as DOX) that induce death in a cell-cycle dependent manner. Therefore, the drug effect is included into the proliferation term $\lambda_p$ (29):

$$\lambda_p = \begin{cases} 0 & \text{outside tumor} \\ \lambda_{M}\sigma(1 - \bar{\lambda}_{effect}G) - \lambda_A & \text{in proliferating tissue} \\ 0 & \text{in hypoxic tissue} \\ -G_N & \text{in necrotic tissue} \end{cases} \tag{13}$$

where $\bar{\lambda}_{effect}$ is the rate of drug-induced cell death, $\lambda_M$ is the mitosis rate, $\lambda_A$ is the apoptosis rate, and $G_N$ is the non-dimensionalized rate of volume loss in necrotic regions assuming that cellular debris is constantly degraded and the resulting fluid is removed (29). For simplicity, the model assumes that proliferation and apoptosis rates are comparable prior to and after therapy, and that cell death is an instantaneous process.

**Numerical Methods**

Briefly, the model equations are solved iteratively at each time step (28). In all equations that involve a diffusion term, a fully nonlinear diffusion solver solves the equation $u(t) = \Delta(D(u, x, y) \cdot \Delta(u) + source(u, x, y)$ in space using centered finite difference approximations and the backward Euler time-stepping algorithm (28, 30). The discretized equations are solved numerically using a nonlinear adaptive Gauss-Seidel iterative method (46, 47). Further details of the numerical solution are in (30) and references therein.

**Statistical Analysis**

Statistical differences were determined by one-way ANOVA. Results were expressed as mean±SE. P-value < 0.05 was considered to indicate statistical significance. Statistical analyses were performed using GraphPad Prism 7 (GraphPad Inc.).

**RESULTS**

**Characterization of SPNCD**

SPNCD containing an $Fe_3O_4$ core and PLGA shell were prepared via co-precipitation method as described previously (12). SEM, TEM, and dynamic light scattering (DLS) characterization of synthesized SPNCD showed that the nanocomposites had a nearly spherical morphology with average diameter of ~120 nm (**Figure 1A** and **1B**).

**SPNCD pH Dependent Degradation and Drug Release**

To assess pH-dependent SPNCD degradation and drug release, SPNCD were suspended in PBS at different pH values. The results (**Figure 1C**) show SPNCD degradation of 17% in 48 h at pH 7.1, whereas degradation was 68% within the same time frame at pH 5.5 ($p < 0.001$). Drug release rates were measured under six pH conditions (**Figure 1D and Supplementary Table 1**). The release was fast at initial timepoints (up to ~5 h), followed by slower release (from ~5 to 48 h).. As expected, SPNCD exhibited pH-dependent drug release profiles, with a significant difference ($p < 0.001$) in release rate between acidic and neutral pH (**Figure 1D**).

**Distribution and Degradation of SPNCD within Tumors**

To experimentally evaluate the distribution of SPNCD within tumor tissue after intra-tumoral injection, Prussian blue staining was used to detect iron in the tissue 24 h after the 5th dose. Thus, the stain represented the spatial localization of SPNCD across the tumor post-injection. (**Supplementary Figure 1A**). It was also observed that SPNCD completely degraded to release iron oxide NPs by day 15 post-injection based on TEM of tumor slices (**Supplementary Figure 1B**), which indicates that the observed MPI signal increase of SPNCD was due to increased Brownian relaxation rates upon release of iron oxide nanoparticles from the polymeric nanocomposite.

**Model Calibration of Drug Effect**

To calibrate the drug effect parameter ($\bar{\lambda}_{effect}$) in the computational model, an avascular

spheroid exposed to DOX in solution was simulated to represent 3D cell culture conditions

(**Supplementary Figure 3**). The simulated DOX and oxygen are shown at therapy start and

after 48 h. DOX concentration is highest near the spheroid periphery due to its limited diffusive

transport into the spheroid. The drug effect (**Table 1**) resulted in a 50% reduction in tumor cells

over 48 h, where the corresponding non-dimensionalized value of DOX was equivalent to a

concentration of 77.35 µM based on previous experiments with MDA-MB-231 breast cancer

cells (45).


**Model-Based Evaluation of Intra-Tumoral SPNCD and Drug Distribution**

To evaluate how differences in vascularity might impact the intra-tumoral distribution of SPNCD

and drug, tumor nodules were simulated growing in time with different levels of vasculature-

induced tissue heterogeneity (**Supplementary Figure 4**). Immediately before therapy

administration, the proliferating tissue fraction is significantly higher for LOW vascular

heterogeneity compared to MEDIUM or HIGH (**Supplementary Figure 5A**), while tumor vessel

surface area (SA) is significantly higher for HIGH vascular heterogeneity compared to MEDIUM

or LOW (**Supplementary Figure 5B**). Images of simulated tumors, tumor acidity, and intra-

tumoral DOX 0, 24, and 48 h following systemic injection, intra-tumoral DOX injection, and intra-

tumoral SPNCD injection are shown in **Figure 2**, where tumors of HIGH vascular heterogeneity

were chosen as representative images. Spatial domain images show differences in DOX

distribution between the 3 administration types. Systemic DOX administration (**Figure 2A**) leads

to drug released into the tissue in proportion to the vascular density. The drug is highest in

proliferating tissue, followed by gradual washout over the next 48 h. Intra-tumoral DOX injection

into the tumor center results in the highest drug concentration immediately post-injection

followed by washout (**Figure 2B**). In contrast, after intra-tumoral SPNCD injection, DOX

concentration in the tumor steadily increases (**Figure 2C**), showing a higher concentration by 24 h post-injection near the tumor center where acidity is highest.  Washout of SPNCD through the vasculature leads to lower concentrations at locations where vessels intersect with tumor or host tissue.

## Model-Based Evaluation of Intra-Tumoral Drug Concentration

Analyses of tumor radius and tumor drug density for each administration type over 14 d from the start of therapy for each level of vascular heterogeneity show that SPNCD pH-dependent drug release resulted in higher intra-tumoral drug concentrations over time (as measured by area-under-the-curve (AUC) values) (**Figure 3**) compared to drug-only administration. Intra-tumoral SPNCD injection delayed tumor regrowth more than systemic or intra-tumoral DOX injections across all levels of vascular heterogeneity. In comparison, intra-tumoral DOX injection resulted in the highest peak concentration of DOX within the tumor occurring at initial time for all levels of heterogeneity, while yielding the lowest effect on tumor growth. Conversely, SPNCD therapy resulted in a delayed rise to the maximum DOX concentration at 1 d post-injection, followed by a slow decline over the following 5 d (**Figure 3**).

## Model-Based Evaluation of Tumor Inhibition due to SPNCD

Drug release and tumor inhibition as a function of treatment type and tumor vascular heterogeneity highlight the value of pH-dependent drug release in the least-vascularized tumor tissue (**Figure 4**). For all cases of vascular heterogeneity, intra-tumoral SPNCD injection yielded higher amounts of drug density within tumor tissue over 14 d post-treatment than either systemically or intra-tumorally injected drug (**Figure 4A**). Yet, as the tumor vascular heterogeneity decreased from HIGH to LOW, the drug density correspondingly increased for SPNCD therapy (from ~64 to ~98 ($\mu$M / mm$^2$)*days) but decreased for systemic DOX (~20 to ~10 ($\mu$M / mm$^2$)*days) and intra-tumoral DOX (~50 to ~44 ($\mu$M / mm$^2$)*days) administrations.

The overall effect on tumor inhibition as a function of time was measured as the tumor radius AUC over the 14-day post-treatment growth period to provide a measure of response to therapy over this timespan. Corresponding to the higher drug densities with SPNCD (**Figure 4A**), the tumor radius AUC trended lower as the vascular heterogeneity decreased (**Figure 4B**). Furthermore, intra-tumoral SPNCD injection significantly decreased the tumor radius AUC for all levels of vascular heterogeneity (8%, 12%, and 25% lower than systemic DOX and 11%, 19%, and 27% lower than intra-tumoral DOX for HIGH, MEDIUM, and LOW vascular heterogeneity, respectively (**Figure 4B**).

The effect of each treatment was also measured by the minimum tumor radius achieved as a fraction of the initial radius, chosen to represent the lowest value attained post-treatment. Intra-tumoral SPNCD yielded 20%, 10%, and 14% lower radius than intra-tumoral DOX for HIGH, MEDIUM, and LOW vascular heterogeneity, respectively; and 13% and 33% lower radius than systemic DOX for MEDIUM and LOW heterogeneity, respectively (**Figure 4C**).  Overall, SPNCD therapy achieved an average minimum tumor radius of 30%, 26%, and 24% for HIGH, MEDIUM, and LOW vascular heterogeneity, respectively, compared to the radius at the start of treatment (**Figure 4C**). These inhibitions are comparable to those observed previously (~20%) with SPNCD treatment *in vivo* (12), which showed that SPNCD significantly inhibit the growth of orthotopic breast tumors without decreasing the body weight of mice over 15 days post injection. The similarity between the experimental and computational data suggests that the model captures sufficient tumor-related parameters to provide realism and insight into tumor inhibition by pH-responsive nanomaterials.

**Effect of Tuning SPNCD Drug Release Rate**

One of the main advantages of nanotechnology-based drug delivery is its tunability. However, it can be challenging to run all the experiments necessary to cover a wide range of tunable factors, such as rate of drug release that can be controlled via chemistry. Instead, if model predictions could yield key insights, experiments could focus on the most interesting sets of tunable factors. Given the match between computational and experimental data, we performed a sensitivity analysis to the SPNCD pH-dependent drug release rate (which depends on the nanomaterial properties) via the computational model to determine *in silico* how engineering the release rate could impact the tumor response to therapy. Taking the experimentally measured release rate (**Figure 1D**) as a baseline, two slower and two faster rates *in silico* were evaluated (**Supplementary Figure 6**) to gauge the effect of this release variation on the simulated tumor response for SPNCD intra-tumoral injection. The tumor drug density and radius over the 14-day growth period after treatment highlight the range of responses for each case of vascular heterogeneity (**Figure 5**). Although the average tumor drug density AUC was variable for each level of vascular heterogeneity (**Figure 6A**), the corresponding average tumor radius AUC (**Figure 6B**) and fraction of initial tumor radius (**Figure 6C**) remained comparable across the different selected SPNCD drug release rates. Slower release rates proved significantly more efficacious than faster rates in terms of tumor radius AUC across all levels of vascular heterogeneity (**Figure 6B**), with LOW heterogeneity having the best response. These findings highlight the consistency of the SPNCD treatment to variation in the pH-dependent drug release rate and suggest that at least with the described set of tumor parameters, the response would be maximized in poorly vascularized tissue.

**DISCUSSION**

This study evaluated a novel technology based on pH-sensitive nanomaterial (SPNCD) with computational modeling to predict therapy response under various tumor conditions, and to compare the results to current standard of care (systemic bolus DOX) and a non-NP mediated control administration (intra-tumoral DOX). Using a 2D tumor model to simulate vascularized breast tumor lesions, the response was evaluated as a function of heterogeneous tissue vascularization and the associated pH. The model was calibrated to previous and current experimental data to ensure biological relevance, and sensitivity analyses were performed on the drug release rate, which depends on the nanomaterial properties. The results show that across a range of vascular heterogeneity from HIGH to LOW, pH-dependent drug release from intra-tumorally injected SPNCD yielded higher drug levels within tumor tissue over 14 d post-treatment than either systemically or intra-tumorally injected drug (**Figure 4A**), with the highest density achieved in the least-vascularized (most deleterious) tumor tissue. Lower vascular heterogeneity would also provide a more homogeneous drug exposure to the tumor tissue. Furthermore, SPNCD treatment yielded the lowest tumor radius AUC over 14 d (**Figure 4B**), with a minimum radius (**Figure 4C**) comparable to that previously observed with mice *in vivo* (12).

Sensitivity analyses of the pH-dependent drug release rate indicate that slower release rates may be more efficacious than faster rates across all levels of vascular heterogeneity (**Figure 6**) since slower rates would extend the timeframe for which tumor cells are exposed to drug. This result suggests that prolonging sustained release may be necessary for maximum benefit from pH-sensitive nanotherapy. This result is consistent with previous computational modeling findings evaluating the performance of pH-sensitive polymer nano-assemblies targeting colorectal cancer, for which slower release was most effective (26). Collectively, the data in this study indicate that prolonged sustained release should also be explored in breast cancer

applications. Future work will need to further evaluate the proposed approach to optimize the antitumor effect of SPNCD by experimentally evaluating modifications to the nanoparticle design, such as adjusting the molecular weight or lactic and glycolic acid ratio of PLGA polymers, which would prolong the drug release. This study provides a first step toward a fully integrated computational and experimental approach that can optimize the antitumor effect of pH-sensitive nanocomposites.

This study evaluated intra-tumoral injection of SPNCD as a means for controlled nanotherapy assessment and which may not translate to clinical practice. Although treatment of cancers by directly injecting tumors with a therapeutic was pioneered by Coley over a century ago,(48) the methodology has not seen wide clinical implementation.  A major reason is that this methodology needs to be customized to the particular tumor conditions, which include size, heterogeneous vascularization, and access to the tumor within the body.  More recently, intra-tumoral injection of immunostimulatory agents has been explored with mixed results (49). The tolerogenic tumor microenvironment, limited accessibility to the tumor location, and the need to wait on the tumor response before proceeding with resection continue to present challenges (49). Ideally, the response could be forecast *a priori* to treatment based on the specific tumor conditions with the goal to design therapy that could maximize this response.

Overall, this study demonstrates how pH-sensitive nanocomposites behave in a heterogeneously vascularized tumor microenvironment, including their drug release rate, sensitivity to pH, and administration route (intra-tumoral vs intravenous injection) with respect to their cytotoxic effect. Interestingly, while intra-tumoral drug-alone was highest for HIGH vascular heterogeneity and lowest for LOW vascular heterogeneity for systemic and intra-tumoral DOX injections, this trend was reversed for SPNCD intra-tumoral injection (**Figure 4A**). These data highlight the suitability of pH-dependent drug release from SPNCD to increase exposure of

poorly vascularized tumor tissue to SPNCD-delivered drug, and may explain why tumor

regrowth is best restrained by the SPNCD therapy.

**CONCLUSIONS**

Although prior work has explored pH-responsive nanoparticles for disease treatment including

cancer (50), this is the first time to our knowledge that this response has been evaluated *in silico*

with respect to the key parameters of tumor vascular heterogeneity and NP drug release rate.

This study is limited in that the model calibration considered one particular $IC_{50}$ (for MDA-MB-

231 cells). Future work will need to evaluate a range of $IC_{50}$ values representative of breast

cancer tumor drug sensitivity. Furthermore, the response only to DOX was evaluated;

conceivably, other chemotherapeutics could be released as payload from SPNC, alone or in

combination. Although intra-tumoral injection has merit for controlled nanotherapy assessment

and may also be of potential clinical utility, in the future the response to SPNCD will need to be

experimentally evaluated via intravenous injection, which is clinically more common.  One

assumption in this study is that SPNCD are stable at neutral pH when not overlapping with the

vasculature. This allows SPNCD to remain indefinitely within the computational model domain,

which guarantees more drug will be released as the tumor regrows and pH decreases in areas

where encapsulated drug is still present. This means that if the post-treatment growth period

were extended beyond 14 d, we anticipate that there would be a larger difference in simulated

tumor radius AUC between SPNCD and DOX treatments. We envision that the detection and

quantification of pH-dependent drug release *in vivo*, e.g., via MPI, will in the future enable

further validation of the modeling results. Longer term, these results could support the ability to

customize pH-sensitive nanotherapy to patient-specific tumor conditions.

**CONFLICT OF INTERESTS**

There are no conflicts to declare.

**ACKNOWLEDGEMENTS**

**AUTHOR CONTRIBUTIONS**

Experimental design and data analysis: YZ, BRS. Computational modeling and data analysis: HAM, HBF. Development of manuscript structure and data presentation: HAM, YZ, BRS, HBF. Writing and revision of the manuscript: HAM, YZ, BRS, HBF. Project administration, resources, and supervision. BRS, HBF.

**TABLES**

**Table 1.** Tumor model main parameters and associated values. All other parameters are as in

(29).

| Parameter | Value | Reference |
|---|---|---|
| Tumor proliferation rate | 1 day$^{-1}$ | Measured (23) |
| Oxygen diffusivity | 1 (*) | (29) |
| Oxygen transfer rate from vasculature | 5 (*) | (29) |
| Oxygen uptake rate by proliferating tumor cells | 1.5 (*) | (29) |
| Oxygen uptake rate by hypoxic tumor cells | 1.3 (*) | (29) |
| Oxygen uptake rate by tumor microenvironment | 0.12 (*) | (29) |
| Oxygen decay rate | 0.35 (*) | (29) |
| Lactate diffusivity | 0.005 (*) | Estimated |
| Lactate production constant (proliferating tissue) | 0.5 (*) | (20) |
| Lactate production constant (hypoxic tissue) | 1 (*) | (20) |
| Lactate production constant (necrotic tissue) | 0 (*) | (20) |
| Lactate washout by vasculature | 0.1 (*) | Estimated |
| Lactate uptake rate | 0.12 (*) | Estimated |
| SPNCD diffusivity | 0.3 (within 0.125 of tumor area from injection site), 0.03 (elsewhere) (*) | Measured (Supplementary Figure 1) |
| SPNCD washout | ~23 min half-life | Measured (Supplementary Figure 2) |
| DOX diffusivity | 2.0 (within 0.125 of tumor area from injection site), 0.2 (elsewhere) (*) | Estimated |
| DOX decay rate | 24 h half-life | Measured (51) |
| DOX *in vitro* IC$_{50}$ (48h) for MDA-MB-231 cells (spheroid culture) | 77.35 µM | Measured (45) |
| DOX release profile from SPNCD | pH-dependent | Measured (Figure 1D) |
| DOX drug effect | 5.3 | Calibrated to IC$_{50}$ |

(*) Value is rescaled by the square of the simulation system characteristic length (1 cm) and divided by the system characteristic time (1 sec) multiplied by the oxygen diffusivity (1 × 10$^{-5}$ cm$^2$ s$^{-1}$) (52). DOX: doxorubicin.

**Table 2.** Levels of tumor tissue heterogeneity based on the thresholds for inducing hypoxia and necrosis. Values for HIGH are based on previously calibrated tumors simulated in (29). Tumor tissue characteristics resulting from these values include viable (proliferating + hypoxic) tumor tissue fraction, necrotic (dead) tissue fraction, and vessel fraction (vascular surface area divided by tumor area).

| Tissue Heterogeneity | Hypoxic Threshold | Necrotic Threshold | Viable Fraction | Hypoxic Fraction | Necrotic Fraction | Vessel Fraction |
|---|---|---|---|---|---|---|
| LOW | 0.405 | 0.4 | 0.73 | 0.09 | 0.18 | 0.018 |
| MEDIUM | 0.485 | 0.48 | 0.76 | 0.07 | 0.17 | 0.021 |
| HIGH | 0.575 | 0.57 | 0.96 | 0.02 | 0.02 | 0.027 |

**FIGURES**
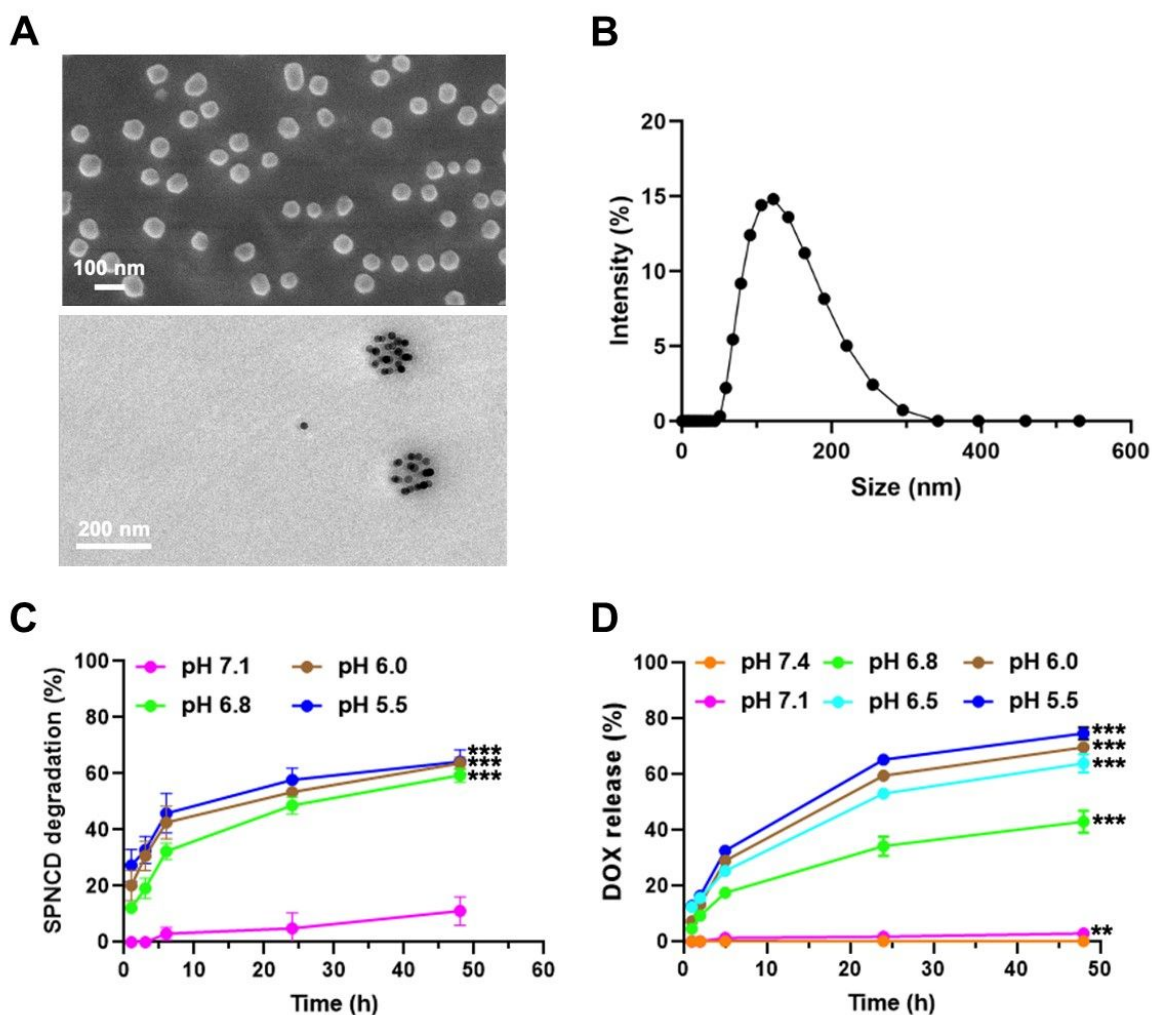


**Figure 1. Experimental SPNCD characterization, and degradation and drug release.** (A) SPNCD scanning electron microscopy (SEM) (top) and transmission electron microscopy (TEM) (bottom). (B) Dynamic light scattering (DLS) of SPNCD. (C) SPNCD degradation over 48 h by measuring size changes through DLS. (D) DOX release from SPNCD over 48 h across various neutral and acidic pH conditions (data shown in Supplementary Figure 1). For both panels, n=3 per group; each group was statistically compared with the pH 7.4 group; **p < 0.01 and ***p < 0.001. As the PLGA shell degrades in acidic pH, DOX release and disassembly of clustered $Fe_3O_4$ nanoparticles in the core occur simultaneously. Mechanistically, disassembly of the clustered core results in increased $Fe_3O_4$ nanoparticle mobility, which is reflected by enhanced

Brownian relaxation (12). This effect contributes to increased MPI signal and the linear

correlation between MPI signal and drug released (12). Color figure online.
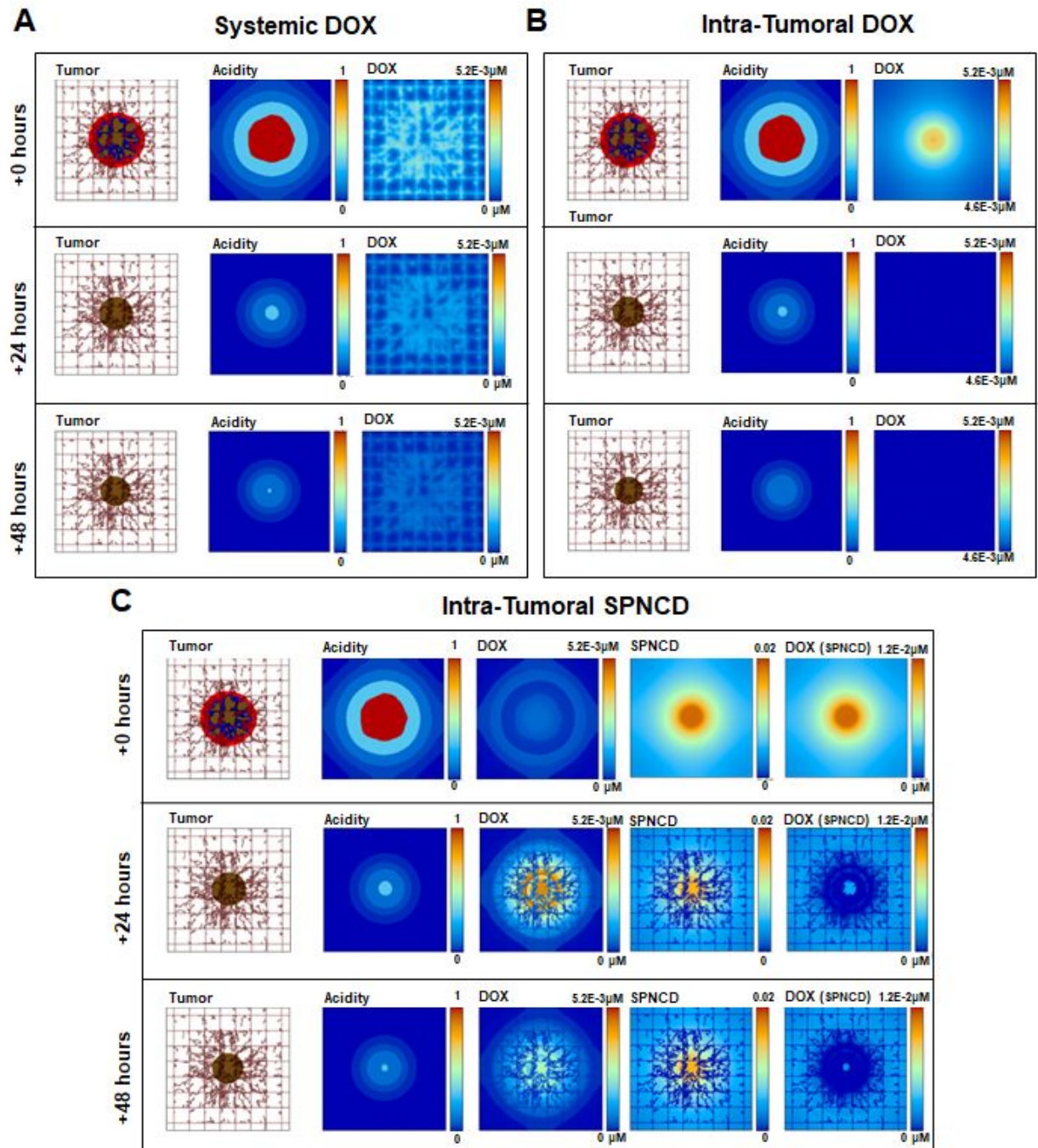
**Figure 2. Distribution of SPNCD and drug after administration of therapy.** Representative images of simulated tumor tissue after (A) systemic DOX administration, (B) intra-tumoral DOX injection, and (C) intra-tumoral SPNCD injection at 0, 24 and 48 h post-therapy. "DOX (SPNCD)" refers to the drug encapsulated within SPNC. Tumors of HIGH vascular heterogeneity were chosen as representative images. In the tumor panels, red denotes

proliferating tissue, blue indicates hypoxic tissue, and brown indicates necrotic tissue. Pre-existing capillary grid is shown as rectangular lines along with sprouts growing due to angiogenesis. Color figure online.
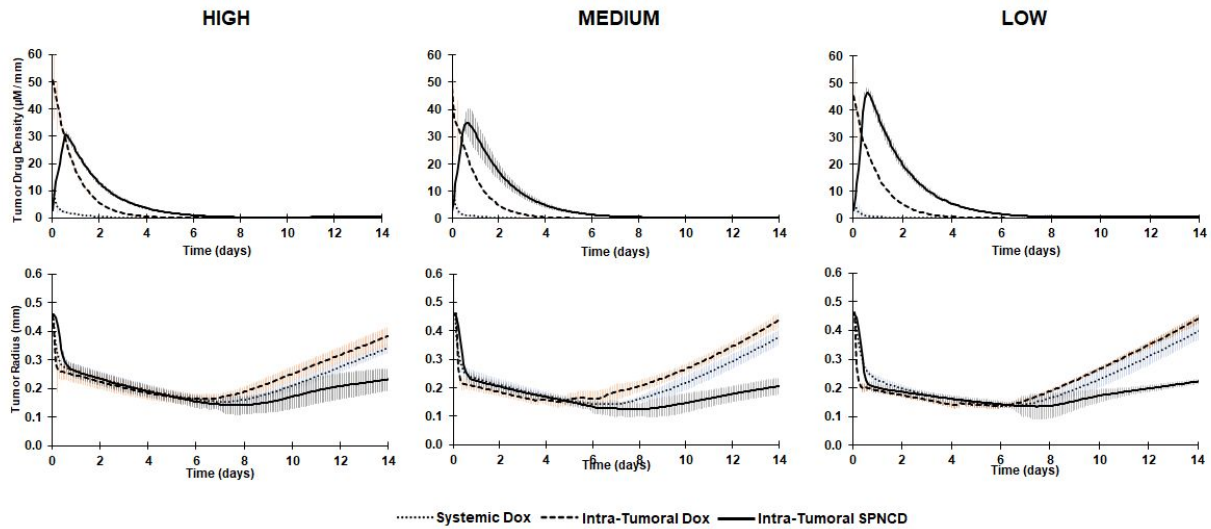
**Figure 3. Computational simulations indicate that intra-tumoral SPNCD injection yields higher drug concentration within tumor tissue and delays tumor growth more than systemic or intra-tumorally injected DOX across three levels of vascular heterogeneity.** Concentration of free DOX within the tumor (top row) varies significantly between administration types as well as tumor radius over time (bottom row) as a function of tumor vascular heterogeneity (ranging from HIGH to LOW). Error bars represent $\pm$ SD. Color figure online.
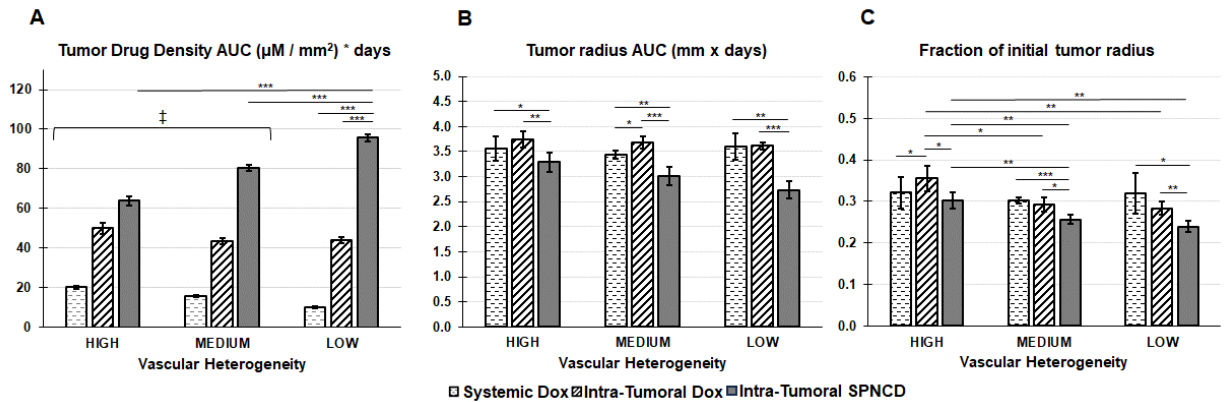
**Figure 4. Computational simulations of intra-tumoral SPNCD injection indicate stronger tumor inhibition than systemic or intra-tumorally injected DOX across three levels of vascular heterogeneity.** (A) Drug within tumor AUC, (B) tumor radius AUC, and (C) smallest fraction of initial tumor radius between administration types and vascular heterogeneities reveal differences in therapy efficacy between the administration types. Error bars represent $\pm$ SD (n=5). *P < 0.05; **P < 0.001; ***P < 0.0001; ‡ all groups P < 0.001. AUC is calculated over 14 d.
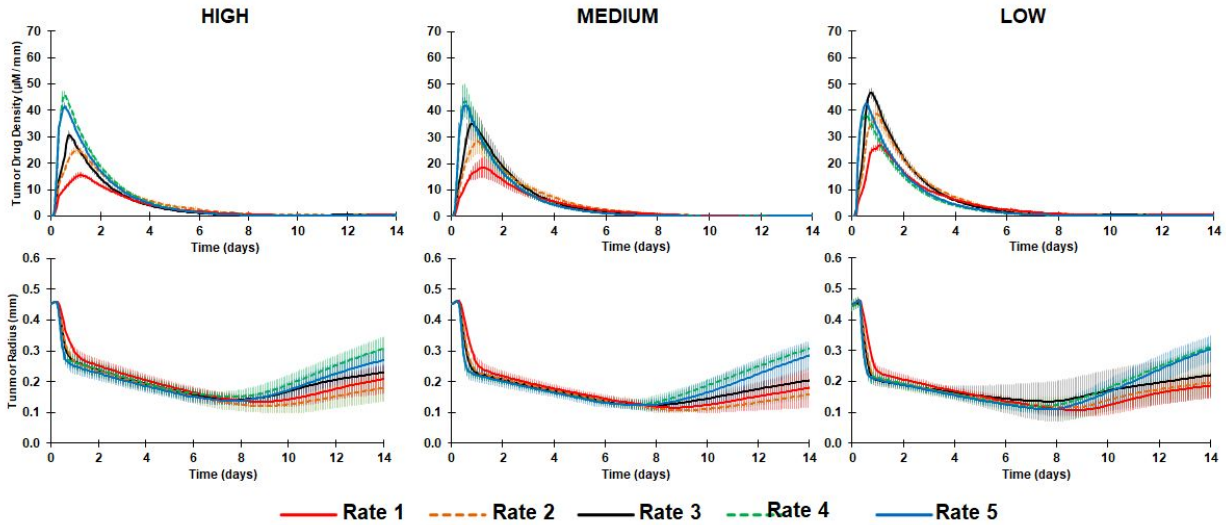
**Figure 5. Computational sensitivity analyses indicate that slower DOX release from intra-tumorally injected SPNCD delays tumor growth more than faster release across three levels of vascular heterogeneity.** Tumor drug density (top row) varies significantly between DOX release rates as well as tumor radius over time (bottom row) as a function of tumor vascular heterogeneity (ranging from HIGH to LOW). Rate 1 is slowest, Rate 2 is slower, Rate 3 is the experimental baseline (**Figure 1D**), Rate 4 is faster and Rate 5 has the fastest DOX release, as defined by the release curves in **Supplementary Figure 6**. Error bars represent $\pm$ SD (n=5). Color figure online.
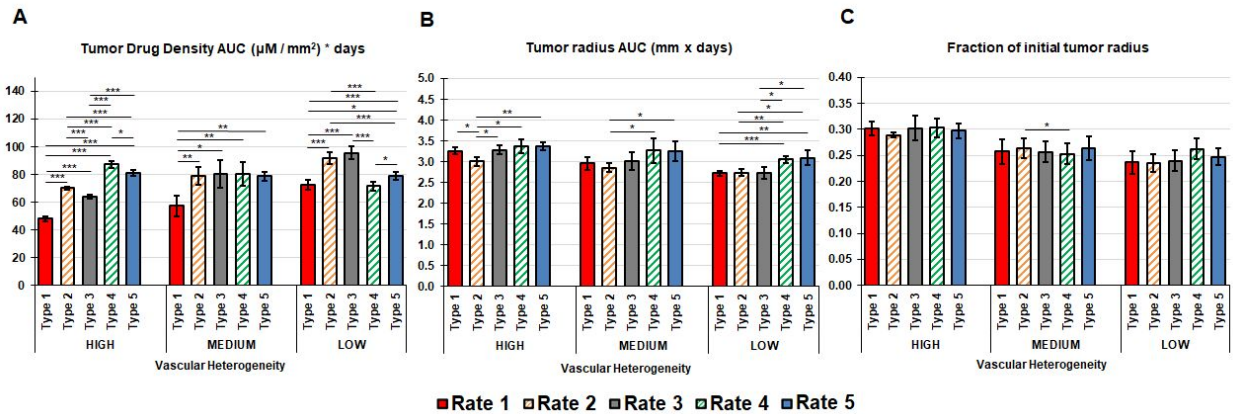
**Figure 6. Computational sensitivity analyses for the vascularity-dependent impact of DOX release rate from intra-tumorally injected SPNCD on tumor inhibition indicate that slower release can improve therapeutic efficacy.** Displayed are (A) tumor drug density, (B) tumor radius AUC, and (C) smallest fraction of initial tumor radius for a range of SPNCD DOX release rates across varying vascular heterogeneity (HIGH to LOW). Rate 1 is slowest, Rate 2 is slower, Rate 3 is the experimental baseline (**Figure 1D**), Rate 4 is faster, and Rate 5 has the fastest DOX release, as defined by the release curves in **Supplementary Figure 6**. Error bars represent $\pm$ SD (n=5). *P < 0.05;  **P < 0.001; ***P < 0.0001.  AUC is calculated over 14 d. Color figure online.

**REFERENCES**

1.      Mu Q, Wang H, Zhang M. Nanoparticles for imaging and treatment of metastatic breast cancer. Expert Opin Drug Deliv. 2017;14(1):123-36.
2.      Baetke SC, Lammers T, Kiessling F. Applications of nanoparticles for diagnosis and therapy of cancer. Br J Radiol. 2015;88(1054):20150207.
3.      Curtis LT, van Berkel VH, Frieboes HB. Pharmacokinetic/pharmacodynamic modeling of combination-chemotherapy for lung cancer. J Theor Biol. 2018;448:38-52.
4.      Sun T, Zhang YS, Pang B, Hyun DC, Yang M, Xia Y. Engineered nanoparticles for drug delivery in cancer therapy. Angew Chem Int Ed Engl. 2014;53(46):12320-64.
5.      Huai Y, Hossen MN, Wilhelm S, Bhattacharya R, Mukherjee P. Nanoparticle Interactions with the Tumor Microenvironment. Bioconjug Chem. 2019;30(9):2247-63.
6.      Tian H, Zhang T, Qin S, Huang Z, Zhou L, Shi J, et al. Enhancing the therapeutic efficacy of nanoparticles for cancer treatment using versatile targeted strategies. J Hematol Oncol. 2022;15(1):132.
7.      Liberti MV, Locasale JW. The Warburg Effect: How Does it Benefit Cancer Cells? Trends Biochem Sci. 2016;41(3):211-8.
8.      Chu S, Shi X, Tian Y, Gao F. pH-Responsive Polymer Nanomaterials for Tumor Therapy. Front Oncol. 2022;12:855019.
9.      Yan Y, Ding H. pH-Responsive Nanoparticles for Cancer Immunotherapy: A Brief Review. Nanomaterials (Basel). 2020;10(8).
10.     Palanikumar L, Al-Hosani S, Kalmouni M, Nguyen VP, Ali L, Pasricha R, et al. pH-responsive high stability polymeric nanoparticles for targeted delivery of anticancer therapeutics. Commun Biol. 2020;3(1):95.
11.     AlSawaftah NM, Awad NS, Pitt WG, Husseini GA. pH-Responsive Nanocarriers in Cancer Therapy. Polymers (Basel). 2022;14(5).
12.     Zhu X, Li J, Peng P, Hosseini Nassab N, Smith BR. Quantitative Drug Release Monitoring in Tumors of Living Subjects by Magnetic Particle Imaging Nanocomposite. Nano Lett. 2019;19(10):6725-33.
13.     Talebloo N, Gudi M, Robertson N, Wang P. Magnetic Particle Imaging: Current Applications in Biomedical Research. J Magn Reson Imaging. 2020;51(6):1659-68.
14.     Curtis LT, Frieboes HB. The Tumor Microenvironment as a Barrier to Cancer Nanotherapy. Adv Exp Med Biol. 2016;936:165-90.
15.     Frieboes HB, Sinek JP, Nalcioglu O, Fruehauf JP, Cristini V. Nanotechnology in cancer drug therapy: a biocomputational approach. In: Ferrari M, Lee AP, Lee LJ, editors. BioMEMS and biomedical nanotechnology: volume I biological and biomedical nanotechnology. 1. New York: Springer US; 2006. p. 435-60.
16.     Hormuth DA, 2nd, Jarrett AM, Lima E, McKenna MT, Fuentes DT, Yankeelov TE. Mechanism-Based Modeling of Tumor Growth and Treatment Response Constrained by Multiparametric Imaging Data. JCO Clin Cancer Inform. 2019;3:1-10.
17.     Phillips CM, Lima E, Woodall RT, Brock A, Yankeelov TE. A hybrid model of tumor growth and angiogenesis: In silico experiments. PLoS One. 2020;15(4):e0231137.
18.     Jarrett AM, Lima E, Hormuth DA, 2nd, McKenna MT, Feng X, Ekrut DA, et al. Mathematical models of tumor cell proliferation: A review of the literature. Expert Rev Anticancer Ther. 2018;18(12):1271-86.
19.     Karolak A, Markov DA, McCawley LJ, Rejniak KA. Towards personalized computational oncology: from spatial models of tumour spheroids, to organoids, to tissues. J R Soc Interface. 2018;15(138).
20.     Miller HA, Lowengrub J, Frieboes HB. Modeling of Tumor Growth with Input from Patient-Specific Metabolomic Data. Ann Biomed Eng. 2022;50(3):314-29.

21.     Dogra P, Butner JD, Chuang YL, Caserta S, Goel S, Brinker CJ, et al. Mathematical modeling in cancer nanomedicine: a review. Biomed Microdevices. 2019;21(2):40.
22.     Frieboes HB, Raghavan S, Godin B. Modeling of Nanotherapy Response as a Function of the Tumor Microenvironment: Focus on Liver Metastasis. Front Bioeng Biotechnol. 2020;8:1011.
23.     Curtis LT, England CG, Wu M, Lowengrub J, Frieboes HB. An interdisciplinary computational/experimental approach to evaluate drug-loaded gold nanoparticle tumor cytotoxicity. Nanomedicine (Lond). 2016;11(3):197-216.
24.     Curtis LT, Wu M, Lowengrub J, Decuzzi P, Frieboes HB. Computational Modeling of Tumor Response to Drug Release from Vasculature-Bound Nanoparticles. PLoS One. 2015;10(12):e0144888.
25.     Leonard F, Curtis LT, Hamed AR, Zhang C, Chau E, Sieving D, et al. Nonlinear response to cancer nanotherapy due to macrophage interactions revealed by mathematical modeling and evaluated in a murine model via CRISPR-modulated macrophage polarization. Cancer Immunol Immunother. 2020;69(5):731-44.
26.     Curtis LT, Rychahou P, Bae Y, Frieboes HB. A Computational/Experimental Assessment of Antitumor Activity of Polymer Nanoassemblies for pH-Controlled Drug Delivery to Primary and Metastatic Tumors. Pharm Res. 2016;33(10):2552-64.
27.     van de Ven AL, Wu M, Lowengrub J, McDougall SR, Chaplain MA, Cristini V, et al. Integrated intravital microscopy and mathematical modeling to optimize nanotherapeutics delivery to tumors. AIP Adv. 2012;2(1):11208.
28.     Wu M, Frieboes HB, McDougall SR, Chaplain MA, Cristini V, Lowengrub J. The effect of interstitial pressure on tumor growth: coupling with the blood and lymphatic vascular systems. J Theor Biol. 2013;320:131-51.
29.     Wu M, Frieboes HB, Chaplain MA, McDougall SR, Cristini V, Lowengrub JS. The effect of interstitial pressure on therapeutic agent transport: coupling with the tumor blood and lymphatic vascular systems. J Theor Biol. 2014;355:194-207.
30.     Macklin P, McDougall S, Anderson AR, Chaplain MA, Cristini V, Lowengrub J. Multiscale modelling and nonlinear simulation of vascular tumour growth. J Math Biol. 2009;58(4-5):765-98.
31.     McDougall SR, Anderson AR, Chaplain MA. Mathematical modelling of dynamic adaptive tumour-induced angiogenesis: clinical implications and therapeutic targeting strategies. J Theor Biol. 2006;241(3):564-89.
32.     Wang ZH, Peng WB, Zhang P, Yang XP, Zhou Q. Lactate in the tumour microenvironment: From immune modulation to therapy. EBioMedicine. 2021;73:103627.
33.     Miller HA, Frieboes HB. Evaluation of Drug-Loaded Gold Nanoparticle Cytotoxicity as a Function of Tumor Vasculature-Induced Tissue Heterogeneity. Ann Biomed Eng. 2019;47(1):257-71.
34.     Rabinowitz JD, Enerback S. Lactate: the ugly duckling of energy metabolism. Nat Metab. 2020;2(7):566-71.
35.     Wu H, Ying M, Hu X. Lactic acidosis switches cancer cells from aerobic glycolysis back to dominant oxidative phosphorylation. Oncotarget. 2016;7(26):40621-9.
36.     Mazzio EA, Boukli N, Rivera N, Soliman KF. Pericellular pH homeostasis is a primary function of the Warburg effect: inversion of metabolic systems to control lactate steady state in tumor cells. Cancer Sci. 2012;103(3):422-32.
37.     Bassi AS, Rohani S, Macdonald DG. Measurement of effective diffusivities of lactose and lactic acid in 3% agarose gel membrane. Biotechnol Bioeng. 1987;30(6):794-7.
38.     Eggleton GP, Hill AV. The coefficient of diffusion of lactic acid through muscle. Proc R Soc Lond B. 1928;103(727):620–8.
39.     Macdougall JDB, McCabe M. Diffusion Coefficient of Oxygen through Tissues. Nature. 1967;215:1173-4.

40.     Pfizer. Doxorubicin Dosage and Administration  [Available from: https://www.pfizermedicalinformation.com/en-us/doxorubicin/dosage-admin.

41.     Cheryl D. Fryar DK-M, Qiuping Gu, Cynthia L. Ogden. National Health Statistics Reports. U.S. Department of Health and Human Services: Centers for Disease Control and Prevention; 2018.

42.     Maximum Allowable Blood Loss OpenAnesthesia 2023 [Available from: https://www.openanesthesia.org/keywords/maximum-allowable-blood-loss/.

43.     Bakker RC, van Es RJJ, Rosenberg A, van Nimwegen SA, Bastiaannet R, de Jong H, et al. Intratumoral injection of radioactive holmium-166 microspheres in recurrent head and neck squamous cell carcinoma: preliminary results of first use. Nucl Med Commun. 2018;39(3):213-21.

44.     Mori V, DuComb EA, Wagner S, Khan F, Bates JHT, Kinsey CM. Visualizing intratumoral injections in lung tumors by endobronchial ultrasound. J Cancer. 2023;14(4):544-53.

45.     Gebeyehu A, Surapaneni SK, Huang J, Mondal A, Wang VZ, Haruna NF, et al. Polysaccharide hydrogel based 3D printed tumor models for chemotherapeutic drug screening. Sci Rep. 2021;11(1):372.

46.     Macklin P, Lowengrub J. Nonlinear simulation of the effect of microenvironment on tumor growth. J Theor Biol. 2007;245(4):677-704.

47.     Macklin P, Lowengrub JS. A New Ghost Cell/Level Set Method for Moving Boundary Problems: Application to Tumor Growth. J Sci Comput. 2008;35(2-3):266-99.

48.     Coley WB. The treatment of malignant tumors by repeated inoculations of erysipelas: with a report of 10 original cases. Am J Med. 1893;105:487–510.

49.     Marabelle A, Andtbacka R, Harrington K, Melero I, Leidner R, de Baere T, et al. Starting the fight in the tumor: expert recommendations for the development of human intratumoral immunotherapy (HIT-IT). Ann Oncol. 2018;29(11):2163-74.

50.     Gao W, Chan JM, Farokhzad OC. pH-Responsive nanoparticles for drug delivery. Mol Pharm. 2010;7(6):1913-20.

51.     Pfizer. Doxorubicin Clinical Pharmacology [Available from: https://www.pfizermedicalinformation.com/en-us/doxorubicin/clinical-pharmacology.

52.     Nugent LJ, Jain RK. Extravascular diffusion in normal and neoplastic tissues. Cancer Research. 1984;44(1):238-44.